bioRxiv preprint doi: https://doi.org/10.1101/810523; this version posted October 20, 2019. The copyright holder for this preprint (which was not certified by peer review) is the author/funder, who has granted bioRxiv a license to display the preprint in perpetuity. It is made available under aCC-BY 4.0 International license.

Midbody remnant inheritance is regulated by the ESCRT subunit CHMP4C

Condensed title: A physical connection between the midbody remnant and the plasma membrane

Authors: Javier Casares-Arias[1], María Ujué Gonzalez[2¶], Alvaro San Paulo[2¶], Leandro N. Ventimiglia[3], Jessica B. A. Sadler[3], David G. Miguez[1,4], Leticia Labat-de-Hoz[1], Armando Rubio-Ramos[1], Laura Rangel[1,5], Miguel Bernabé-Rubio[1], Jaime Fernández-Barrera[1], Isabel Correas[1,5], Juan Martín-Serrano[3] and Miguel A. Alonso[1*]

Affiliations: [1]Centro de Biología Molecular Severo Ochoa, Consejo Superior de Investigaciones Científicas and Universidad Autónoma de Madrid, [2]Instituto de Micro y Nanotecnología, Consejo Superior de Investigaciones Científicas, [3]Department of Infectious Diseases, Faculty of Life Sciences and Medicine, King's College London, [4]Department of Condensed Matter Physics and [5]Department of Molecular Biology, Universidad Autónoma de Madrid

Keywords: Midbody remnant; ESCRT complex; primary cilium; polarized epithelial cells; cytokinesis

***Corresponding author:** maalonso@cbm.csic.es

[¶]Equal contribution

Abbreviations: CHMP, charged multivesicular body protein; CLEM, correlative light and electron microscopy; ESCRT, endosomal sorting complex required for transport; FB, Flemming body; MB, midbody; MBR, midbody remnant; SEM, scanning electron microscopy; VLV, very-low-voltage

bioRxiv preprint doi: https://doi.org/10.1101/810523; this version posted October 20, 2019. The copyright holder for this preprint (which was not certified by peer review) is the author/funder, who has granted bioRxiv a license to display the preprint in perpetuity. It is made available under aCC-BY 4.0 International license.

Abstract

The inheritance of the midbody remnant (MBR) breaks the symmetry of the two daughter cells, with functional consequences for lumen and primary cilium formation by polarized epithelial cells, and also for development and differentiation. However, despite their importance, neither the relationship between the plasma membrane and the inherited MBR nor the mechanism of MBR inheritance is well known. Here, the analysis by correlative light and ultra-high-resolution scanning electron microscopy reveals a membranous stalk that physically connects the MBR to the apical membrane of epithelial cells. The stalk, which derives from the uncleaved side of the midbody, concentrates the ESCRT machinery. The ESCRT CHMP4C subunit enables MBR inheritance, and its depletion dramatically reduces the percentage of ciliated cells. We demonstrate: (1) that MBRs are physically connected to the plasma membrane, (2) how CHMP4C helps maintain the integrity of the connection, and (3) the functional importance of the connection.

bioRxiv preprint doi: https://doi.org/10.1101/810523; this version posted October 20, 2019. The copyright holder for this preprint (which was not certified by peer review) is the author/funder, who has granted bioRxiv a license to display the preprint in perpetuity. It is made available under aCC-BY 4.0 International license.

Introduction

The midbody (MB) is the narrow bridge that connects the two nascent daughter cells resulting from animal cell division. MB cleavage results in the physical separation of the cells, through a process known as abscission, and in the formation of an MB remnant (MBR) (Fededa and Gerlich, 2012, Mierzwa and Gerlich, 2014). Increasing evidence indicates that, instead of being an abscission byproduct, the MBR assumes important roles in development and differentiation (Chen et al., 2013). In polarized renal epithelial cells, the MBR licenses the centrosome to assemble the primary cilium, which is a solitary plasma membrane protrusion involved in the regulation of multiple developmental signaling pathways (Bernabe-Rubio et al., 2016, Bernabé-Rubio et al., 2019), and defines the location of the apical membrane during lumen formation (Lujan et al., 2017).

The MB is continuous with the plasma membrane and consists of an electron-dense central region called the Flemming body (FB) (Byers and Abramson, 1968), which comprises anti-parallel microtubule bundles. Flanking the FB, the MB has two arms, containing parallel microtubule bundles, vesicles and protein factors, that bridges the two daughter cells. In principle, when severing occurs on both arms, the MBR becomes extracellular and it can remain free in the extracellular milieu, or stay attached to the surface of one of the daughter cells. or of a neighboring cell, or be eliminated. However, severing on just one arm should lead to the MBR to be inherited by the cell on the opposite side, although this has not been well documented experimentally (Schiel et al., 2011). Given the importance of the MBR, it seems inevitable that its fate must be tightly regulated (Ou et al., 2014, Dionne et al., 2015). However, despite the enormous effort expended on trying to understand the mechanism of the first cleavage of the MB, which marks the end of the abscission process, little attention has been paid to the inheritance of the connected MBRs and, thus, to the regulation of the cut of the membrane of the other MB arm.

In this study, using ultra-high-resolution scanning electron microscopy (SEM), we demonstrate the existence of the physical continuity between the MBR membrane and the plasma membrane of Madin-Darby canine kidney (MDCK) cells, and show that only one side of the MB is cleaved in most cases. We find that, once abscission is completed, the charged multivesicular body protein (CHMP) 4C subunit of the endosomal sorting complex required for transport (ESCRT) complex delays the

bioRxiv preprint doi: https://doi.org/10.1101/810523; this version posted October 20, 2019. The copyright holder for this preprint (which was not certified by peer review) is the author/funder, who has granted bioRxiv a license to display the preprint in perpetuity. It is made available under aCC-BY 4.0 International license.

cleavage of the membrane of the other arm, allowing the MBR to remain on the cell surface as an organelle physically connected to the rest of the plasma membrane. The connection enabless the MBR to license the centrosome for primary cilium assembly, and might be also important in other processes involving the MBR.

bioRxiv preprint doi: https://doi.org/10.1101/810523; this version posted October 20, 2019. The copyright holder for this preprint (which was not certified by peer review) is the author/funder, who has granted bioRxiv a license to display the preprint in perpetuity. It is made available under aCC-BY 4.0 International license.

Results

MBRs of MDCK cells are connected to the plasma membrane by a membranous extension

Epithelial MDCK cells constitute a paradigm of polarized epithelial cell (Rodriguez-Boulan et al., 2005). Given the important role of the MBR in MDCK cells, we chose this cell line as a model cell system to study whether there was continuity between the MBR and the rest of the cell. Unlike tumor-derived cell lines (Kuo et al., 2011, Ettinger et al., 2011), MDCK cells have a single MBR at most (Bernabe-Rubio et al., 2016, Bernabé-Rubio et al., 2019). Quantitative analysis indicates that >95% of MBRs are on the apical surface (Fig. S1A). Super-resolution structured illumination microscopy showed that MBRs are formed by the FB, which was visualized with the marker MKLP1, flanked by two small microtubule pools (Fig. 1A). It is of note that, unlike previous stages of the abscission process (Fig. S1B), the MBR did not show large microtubule bundles flanking the FB (Fig. 1A).

Abscission requires both the membrane and microtubules to be severed. Loss of tubulin staining on one side of the FB, coupled with the retraction of the structure, is considered a reliable indicator of the first membrane cleavage event. On the other side of the FB, however, additional techniques should be used to ascertain the integrity of the remaining membranous MB arm. SEM is a powerful tool for examining cell-surface topography. The most recent generation microscopes equipped with field emission tips and very-low-voltage (VLV) operation capabilities (incidence electron beam energy $E_0 \leq 1$ keV) allow direct, high-resolution imaging of cells on glass substrates without the need for metal coating (Wuhrer and Moran, 2016). To investigate the existence of a membranous stalk connecting the MBR membrane and the plasma membrane, we used correlative light microscopy and VLV SEM (CLEM) in subconfluent cultures of cells stably expressing GFP-tubulin (Fig. S1C, D). Light microscopy, on the one hand, allows selection of MBR candidate structures by the strong labeling of the FB with GFP-tubulin, discarding native MBs or MB-derived structures that still maintain microtubule bundles flanking the FB. Inspection of the candidate structures by VLV SEM, on the other hand, identified unambiguously *bona fide* MBRs by their typical morphology (87 of 117 structures analyzed). As revealed by CLEM, MBRs have a morphology consisting of a central "core" region, which corresponds to the bulge observed by transmission EM that contains the FB (Byers and Abramson, 1968),

bioRxiv preprint doi: https://doi.org/10.1101/810523; this version posted October 20, 2019. The copyright holder for this preprint (which was not certified by peer review) is the author/funder, who has granted bioRxiv a license to display the preprint in perpetuity. It is made available under aCC-BY 4.0 International license.

flanked by two opposed conical structures (Fig. 1B). In top-view images, some of the MBRs examined have an evident membranous connection, emerging from one of the cones, with the plasma membrane (Fig. 1B, left panel) that is absent from other MBRs (Fig. S1E, left panel). After acquisition of a top-view image, the sample stage was tilted through 45º and rotated (Fig. S1F), making it possible to observe the MBR from different angles (right panels in Fig. 1B and Fig. S1E). We reasoned that the connection should restrict MBR movement in live cells in such a way that the MBR could move, defining a funnel-shaped volume whose narrowest end coincides with the connection point (Fig. 1C). To confirm the existence of the connection, we carried out time-lapse analysis of MBR movement and observed that this was the case (Fig. 1D, E and Video 1). In summary, the two independent experimental approaches used support the existence of a physical connection between some MBRs and the plasma membrane.

The membranous connection extends from the tip of the largest MBR cone

The MBRs identified in our analysis were quantified and classified according to the existence of a membranous connection with the plasma membrane, the symmetry between the two cones, and the size of the cone from which the connection arises (Fig. 2A, B). Top-view SEM images showed a clear connection with the plasma membrane in 45/87 of the MBRs, whereas no discernible connection was found in 17/87 MBRs (Fig. 2B). The remaining MBRs were classified as “unclear” because of their arrangement on the cell surface precludes the visualization of the possible connection in top-view images (Fig. S2A). The number of “informative” (45 + 17) top-view images of MBRs was considered sufficient to make further analysis of unclear cases unnecessary. The inclination angle formed by the long axis of the MBR and the cell surface observed for the unclear cases was more similar to that of the clearly connected MBRs than to those of the non-connected ones (Fig. S2B, C), suggesting the presence of a connection in most of the unclear cases. This observation implies that the observed fraction of connected MBRs with respect to the total “informative” cases (45/62) is likely an underestimate of the genuine fraction of connected MBRs.

A morphological feature of MBRs is the apparent degeneration of one of the cones. While one cone tends to have a defined form and size, the other is frequently shorter and rounder, giving rise to an asymmetrical MBR (Fig. 2A). It is of note that the connection arose from the larger cone in most (19/22) of the connected MBRs with asymmetrical cones (Fig. 2B).

bioRxiv preprint doi: https://doi.org/10.1101/810523; this version posted October 20, 2019. The copyright holder for this preprint (which was not certified by peer review) is the author/funder, who has granted bioRxiv a license to display the preprint in perpetuity. It is made available under aCC-BY 4.0 International license.

To characterize the MBR, we measured the dimensions of the MBR using top-view SEM images. The FB has a homogeneous width regardless of the existence of a connection. Connected MBRs were longer and more variable in length than the non-connected ones, being the connected side longer than the opposite one (Fig. S2D, E). Independent measurements of the length based on MBR movement yielded similar values, supporting the validity of this approach (Fig. S2F-H).

In conclusion, the analyses presented so far indicate that MBRs display a number of prevalent structural features, the most common one being the presence of a membranous stalk presumably derived from the unresolved side of the bridge, which most often coincides with the largest cone, physically connecting the MBR membrane to the plasma membrane.

The ESCRT machinery concentrates at the connection between the MBR and the plasma membrane

The final steps of the abscission process are carried out by the ESCRT machinery (Carlton and Martin-Serrano, 2007, Morita et al., 2007, Schoneberg et al., 2017), which progressively accumulates into rings at both sides of the FB (Elia et al., 2011). ESCRT-III assembles spiral polymers whose diameter decreases as they grow away from the FB, constricting the MB to the limit allowed by the microtubules inside. After microtubule clearance, the ESCRT polymer remodels generating a second ESCRT pool that is positioned at the future cleavage site (Elia et al., 2012, Goliand et al., 2018).

To investigate the involvement of ESCRT-III proteins in the cleavage of the membrane of the other MB arm, we expressed GFP-fused forms of the ESCRT proteins CHMP4B (GFP-L-CHMP4B) and CHMP4C (GFP-L-CHMP4C), and analyzed their localization before and after the end of the abscission process. These proteins, in which GFP is separated from CHMP4C and CHMP4B by a 25-nm long flexible linker, were previously shown to have the expected localization at the midbody, and their expression did not delay midbody abscission time (Ventimiglia et al., 2018, Sadler et al., 2018). Both proteins first accumulated in ring-like structures on both sides of the FB and then polymerized towards the abscission site, resulting in the appearance of cone-shaped staining in one of the MB arms. Once microtubules were cleared from this arm, membrane cleavage and, consequently, daughter cell separation occurred. After abscission, CHMP4B, CHMP4C and microtubules followed essentially the same sequence of events on the other side of the FB, generating an MBR (Fig. 3A,B; Fig.

bioRxiv preprint doi: https://doi.org/10.1101/810523; this version posted October 20, 2019. The copyright holder for this preprint (which was not certified by peer review) is the author/funder, who has granted bioRxiv a license to display the preprint in perpetuity. It is made available under aCC-BY 4.0 International license.

S3A,B). The same was observed in a panel of endogenous ESCRT proteins (Fig. S3B). All MBRs contained ESCRT proteins (Fig. S3C) but the pattern of distribution was not the same in all MBRs. The MBRs that presented a similar pattern on both sides of the FB, mainly with staining only on the FB rims, were classified as "even" MBRs, whereas those that, in addition to the FB rims, had a second ESCRT pool in only one side of the FB were categorized as "uneven" MBRs. The second ESCRT pool in the uneven MBRs adopted the form of a cone, filament or dot (Fig. 3A, B; Fig. S3D). Quantitative analysis revealed that most MBRs display uneven ESCRT distribution (Fig. 3C). It is of particular note that the MBR side with the extra ESCRT pool coincides with that having the membranous stalk. This pool is present in a region of the connection proximal to the plasma membrane, as determined by CLEM of cells stably expressing Cherry-tubulin and GFP-L-CHMP4C (Fig. 3D-F) or GFP-L-CHMP4B (Fig. 3F; Fig. S3E, F). Supporting this localization, time-lapse analysis of MBR movement showed that the pool remained immobile, as may be seen in the projected kymograph, whereas the distal pool, which corresponds to the FB rims, moved drawing a circle around it (Fig. 3G).

In summary, ESCRT proteins localize to the membranous stalk that connects the MBR to the plasma membrane and have a similar distribution to that found in pre-abscission stages right before the MB arm is first cleaved (Goliand et al., 2018). Since the presence of an ESCRT pool distant from that surrounding the FB has been associated with the last stage of membrane cleavage (Goliand et al., 2018), we proceeded to analyze how the cleavage of the connection is prevented.

CHMP4C depletion reduces the percentage of cells with an MBR and impairs primary ciliogenesis

The abscission checkpoint delays abscission by regulating the ESCRT machinery in the case of mitotic problems, such as persisting chromatin within the bridge, incomplete nuclear pore reformation, or tension in the bridge produced by opposite pulling forces from the daughter cells (Agromayor and Martin-Serrano, 2013, Caballe et al., 2015). The activation of the abscission checkpoint retards abscission by promoting the phosphorylation of the ESCRT-III subunit CHMP4C by the kinase Aurora B, Ser210 being the major phospho-acceptor residue (Carlton et al., 2012). To investigate the involvement of this mechanism in the regulation of the second cleavage of the MB, we used specific siRNA (siCHMP4C) to knockdown CHMP4C expression (Fig. S4A,

bioRxiv preprint doi: https://doi.org/10.1101/810523; this version posted October 20, 2019. The copyright holder for this preprint (which was not certified by peer review) is the author/funder, who has granted bioRxiv a license to display the preprint in perpetuity. It is made available under aCC-BY 4.0 International license.

B). As a control, we observed that CHMP4C knockdown accelerated abscission without affecting the number of dividing cells (Fig. 4A and Fig. S4C), as has been previously been noted in other cell lines (Carlton et al., 2012, Sadler et al., 2018, Caballe et al., 2015). It is of note that the percentage of cells with an MBR was much lower in cells deficient in CHMP4C expression (Fig. 4B, S4E, F), being >95% of the MBRs on the cell surface as they are in control cells (Fig. S1A). This result argues against the possibility that the loss of MBRs in CHMP4C-deficient cells was due to MBR internalization and degradation. The CHMP4C mutants S210A and A232T, which is a CHMP4C allele associated with increased susceptibility to cancer, are unable to replace endogenous CHMP4C in abscission regulation (Carlton et al., 2012, Sadler et al., 2018). The effect of CHMP4C knockdown was rescued by the exogenous expression of siCHMP4C-resistant forms of GFP fusions of wild type but not of the S210A and A232T CHMP4C mutants (Fig. 4B and Fig. S4D-F). The percentage of MBRs positive for the mutants (Fig. S4G), their distribution within the MBR (Fig. S4H), and the total number of cells per field (Fig. S4I) were similar to those of the wild-type CHMP4C protein (Fig. 3C, Fig. S3C, Fig. S4I). As a control, we observed that the number of cells connected by a midbody decreased in siCHMP4C-treated cells and that this effect was corrected by the intact protein but not by the S210A or A232T CHMP4C mutants (Fig. S4J). The results illustrated in Fig. 4A,B and Fig. S4 are similar to those reported for CHMP4C in the control of the first cut of the MB membrane by the abscission checkpoint mechanism (Carlton et al., 2012, Capalbo et al., 2012) and suggest that CHMP4C has a similar role in the second cut.

Since the MBR licenses primary cilium formation in polarized epithelial cells (Bernabe-Rubio et al., 2016), we examined the effect of CHMP4C knockdown on this process. We observed a dramatic drop in the percentage of ciliated cells (Fig. 4C, D), which is consistent with the loss of MBRs in CHMP4C-deficient cells (Fig. 4B). This result is in agreement with a previous report showing that the physical removal of the MBR greatly reduces primary ciliogenesis (Bernabe-Rubio et al., 2016) and further highlights the importance of the MBR in this process by providing a genetic evidence of the requirement for MBR in primary cilium formation by polarized epithelial cells.

bioRxiv preprint doi: https://doi.org/10.1101/810523; this version posted October 20, 2019. The copyright holder for this preprint (which was not certified by peer review) is the author/funder, who has granted bioRxiv a license to display the preprint in perpetuity. It is made available under aCC-BY 4.0 International license.

Discussion

Although the FB was first described more than 125 years ago, the discovery of its role in abscission is relatively recent, and even more so is the evidence of important post-mitotic roles for the MBR (Chen et al., 2013). Accumulation of MBRs has been associated with increased cell reprogramming efficiency of stem cells and *in vitro* tumorigenicity of cancer cells (Kuo et al., 2011, Ettinger et al., 2011). In polarized epithelial cells, the MBR meets the centrosome at the center of the apical membrane and enables the centrosome for primary cilium formation (Bernabe-Rubio et al., 2016). Using CLEM, we identified a membranous stalk in polarized epithelial MDCK cells that physically connects the MBR membrane and the plasma membranes of most MBR-containing cells. The stalk is derived from the unresolved side of the bridge and contains ESCRT machinery, including the regulatory subunit CHMP4C. The knockdown of CHMP4C expression causes the loss of the MBR and, consistent with its role in primary cilium formation, a dramatic reduction in the percentage of ciliated cells. These results indicate that an MBR physically connected to the plasma membrane by a membranous stalk, whose integrity is regulated by CHMP4C, is the form of MBR used by MDCK cells to license primary ciliogenesis.

We first identified candidate MBR structures from the presence of GFP-tubulin in the MB core and its absence from the two MB arms. The selected structures were analyzed in a state-of-the-art, VLV SEM using samples that were prepared by a gentle procedure (Katsen-Globa et al., 2016) omitting conductive coating. This equipment revealed the subnanometric topography of MBRs, which enabled structures without the typical MBR morphology to be discounted. Using this approach, we visualized a membranous stalk between the MBR and the plasma membrane in a large proportion of MBRs. However, such a connection was not observed in a previous CLEM study (Crowell et al., 2014) that combined phase-contrast microscopy to identify MBR candidates, sample preparation by standard procedures, and analysis under conventional SEM equipment (Fremont and Echard, 2017). The discrepancy between the two studies might be due to the different cell lines analyzed —HeLa cells in Crowell et al. (2014) and MDCK cells in ours— or to the distinct protocols for sample preparation and the SEM equipments used. In addition to detecting the connection, our CLEM analysis revealed that one of the MBR cones is larger than the other, likely because the shorter one results from the degeneration of the cone on the side where abscission occurs.

bioRxiv preprint doi: https://doi.org/10.1101/810523; this version posted October 20, 2019. The copyright holder for this preprint (which was not certified by peer review) is the author/funder, who has granted bioRxiv a license to display the preprint in perpetuity. It is made available under aCC-BY 4.0 International license.

Consistent with this possibility, we observed that the connecting stalk most often arises from the largest cone of the MBR. The presence of a membranous connection with the plasma membrane in MBRs argues against the use of the loss of microtubules on both sides of the FB as an indicator of bilateral MB membrane cleavage. In addition, the use of phase-contrast microscopy cannot distinguish between connected and unconnected MBRs because the connection is very small. Therefore, cautious must be exercised when such criteria are the only ones used to assess the second cleavage of the MB membrane.

We observed that most MBRs contained ESCRT polymers only on the side corresponding to the largest cone, similar to those present just before the first cleavage of the MB membrane. We mapped the ESCRT pool at the membranous connection between the MBR and the plasma membrane by CLEM, and confirmed the localization by analyzing the MBR motion. This location of ESCRT proteins is consistent with the presence of helical filaments in the unresolved MB arm, as observed by soft X-ray cryotomography (Sherman et al., 2016). This pool contains CHMP4C, which is a crucial component of the checkpoint mechanism that delays abscission when mitotic problems occur. In those cases, the knockdown of CHMP4C accelerates abscission and only the expression of wild type CHMP4C but not of the CHMP4C S210A or A232T mutants can substitute the endogenous protein to delay membrane cleavage. Since the number of cells with an MBR was greatly diminished in CHMP4C-knockdown cells and the effect was corrected by expression of intact CHMP4C but not by CHMP4C mutants, we propose that, similar to its role in the abscission checkpoint (Carlton et al., 2012, Capalbo et al., 2012), CHMP4C allows MBRs to remain connected to the plasma membrane by delaying the cleavage of the connection.

Our previous study on primary cilium biogenesis indicated that the MBR prepares the centrosome for primary cilium assembly in cells, such as MDCK cells, in which the primary cilium is entirely assembled in the plasma membrane (Bernabe-Rubio et al., 2016). The existence of the physical connection might facilitate the directional movement of the MBR to the middle of the apical membrane to meet the centrosome by direct anchoring to the cytoskeleton. In addition, the continuity of the MBR with the rest of the plasma membrane makes possible the delivery of MBR-associated membranes to the centrosome for the assembly of the ciliary membrane (Bernabé-Rubio et al., 2019). Since we found that a functional consequence of the loss

bioRxiv preprint doi: https://doi.org/10.1101/810523; this version posted October 20, 2019. The copyright holder for this preprint (which was not certified by peer review) is the author/funder, who has granted bioRxiv a license to display the preprint in perpetuity. It is made available under aCC-BY 4.0 International license.

of the connection caused by CHMP4C silencing is the impairment of primary ciliogenesis, we conclude that the connection is required to prepare the centrosome for primary ciliogenesis.

The relationship between the MBR membrane and the plasma membrane resembles that of the primary cilium, since the ciliary membrane is continuous with, but different from, the rest of the plasma membrane. The ciliary membrane harbors a large variety of important receptors for cell signaling, including receptors involved in cell growth, migration, development and differentiation (Gerdes et al., 2009, Ishikawa and Marshall, 2011, Singla and Reiter, 2006). Given the continuity of the MBR membrane and the plasma membrane, it could be that the remnant of an ancient cytokinetic intercellular bridge developed some of the ciliary functions before the cilium emerged during evolution, and that the remnant itself promoted the transition by facilitating the appearance of the cilium through a mechanism reminiscent of its role in primary cilium formation in polarized epithelial cells.

In conclusion, our study reveals that the majority of MBRs inherited in MDCK cells are physically connected to the plasma membrane through a membranous stalk derived from the unresolved side of the cytokinetic bridge. The ESCRT subunit CHMP4C controls the integrity of the other MB arm to ensure the continuity between the MBR membrane and the plasma membrane and, in this way, the MBR facilitates primary cilium formation.

bioRxiv preprint doi: https://doi.org/10.1101/810523; this version posted October 20, 2019. The copyright holder for this preprint (which was not certified by peer review) is the author/funder, who has granted bioRxiv a license to display the preprint in perpetuity. It is made available under aCC-BY 4.0 International license.

Materials and Methods

Antibodies. The sources of the antibodies to the different markers were as follows: total α-tubulin (mouse mAb IgG1, clone DM1A, product T6199; used at 1/5,000), tyrosinated α-tubulin (rat mAb IgG2a, clone YL1/2, product MAB1864; used at 1/200), acetylated tubulin (mouse mAb IgG2b; clone 6-11-B1, product T7451; used at 1/500) and CHMP1B (rabbit polyclonal antibody, ATLAS product HPA061997; used at 1/500) were from Merck; CHMP2A (rabbit polyclonal, product 10477-1-AP; used at 1/500) was from Proteintech; CHMP1A (rabbit polyclonal, product ab178686; used at 1/500) was from Abcam; PRC1 (mouse mAb IgG2b, clone 16F2, product MA1-846; used at 1/100) was from ThermoFisher Scientific; MKLP1 (rabbit polyclonal, product sc-867; used at 1/100) was from Santa Cruz; GFP (mouse mAbs IgGκ, mixture of clones 7.1 and 13.1, product 11814460001; used at 1:1,000) was from Roche. The rabbit polyclonal antibody to CHMP4C was prepared by Lampire Biologicals and used at 1/200. The rabbit polyclonal antibodies to ALIX (used at 1/500) and IST1 (used at 1/1,000) (Bajorek et al., 2009) were generous gifts from Wesley Sundquist (University of Utah). Secondary antibodies conjugated to Alexa-488, -594 or -647 were from Thermo Fisher Scientific.

Cell culture. Epithelial canine MDCK II (CRL2936) cells were obtained from the ATCC and grown in MEM supplemented with 5% FBS (Merck) at 37°C in an atmosphere of 5% CO_2. Mycoplasma testing was regularly performed. For immunofluorescence and quantitative analysis, 3.0×10^4 cells were plated onto coverslips maintained in 24-well multiwell plates and grown for 48 h. For correlative light and electron microscopy and time-lapse studies 1.5×10^5 cells were plated onto 35-mm glass-bottom plates (MatTek) and grown for 48 h.

DNA constructs, siRNA and transfection conditions. The DNA constructs expressing EGFP- or mCherry-tubulin were from Takara Bio, Inc. MDCK II cells stably expressing these proteins were generated by transfection of 1.0×10^6 cells with Amaxa Nucleofector II (Lonza) using the L-005 program. After selection with 2 mg/ml G-418 (Thermo Fisher Scientific), the resulting clones were screened under a fluorescence microscope. The retroviral constructs pNG72-GFP-L-CHMP4B, pNG72-GFP-L-CHMP4C, pNG72-GFP-L-CHMP4C A232T have been described previously (Ventimiglia et al., 2018, Sadler et al., 2018). pNG72-GFP-L-CHMP4C S210A was generated by site-directed mutagenesis using a commercial kit (Quickchange Lightning, Agilent Technologies).

bioRxiv preprint doi: https://doi.org/10.1101/810523; this version posted October 20, 2019. The copyright holder for this preprint (which was not certified by peer review) is the author/funder, who has granted bioRxiv a license to display the preprint in perpetuity. It is made available under aCC-BY 4.0 International license.

For retroviral production, 293T cells were co-transfected with the indicated retroviral construct and with the retroviral packaging vectors, MLV-GagPol/pHIV 8.1 and pHIT VSVg at a ratio of 2:3:1 for 48 h using polyethylenimine (Polysciences, Germany). 293T supernatant was collected and filtered through a 0.2-μm filter before being used to transduce MDCK II cells. For siRNA assays, $3.0x10^4$ cells were transfected with 100 nM siRNA non-targeting (siNT) or custom siRNA targeted to dog CHMP4C (siCHMP4C, 5'- CTCGCTCAGATTGATGGCACA-3'; ThermoFisher Scientific) (Carlton et al., 2012) using Lipofectamine 2000 (Thermo Fisher Scientific) according to the manufacturer's recommendations. Cells were transfected twice, 48 h and 6 h before the beginning of the experiments. The pSuperGFP-shCHMP4C construct, which expresses GFP and shRNA to dog CHMP4C simultaneously from independent promoters, was generated by cloning a synthetic DNA duplex with the same target sequence as siCHMP4C into the pSuper plasmid (OligoEngine). The resulting plasmid was combined with the plasmid pEGFP-N1 using the unique EcoO109I and Afl III sites present in both plasmids.

Confocal microscopy. Cells were fixed in cold methanol for 5 min and blocked with 3% (wt/vol) BSA for 30 min. Cells were incubated with the indicated primary antibodies at 4ºC overnight, and were washed and then stained with the appropriate fluorescent secondary antibodies. Coverslips were mounted using ProLong Gold antifade reagent (ThermoFisher Scientific). Super-resolution images were obtained using a Nikon N-SIM-S superresolution microscope with a 100x oil immersion objective (Numerical aperture, NA, of 1.49) and processed with NIS-Elements. A stack containing the whole cell was acquired in 3D-SIM imaging mode. Maximum intensity projections of the entire stack are shown. Images for ESCRT localization analysis were acquired with an LSM 800 confocal microscope (Zeiss) equipped with a 63x oil immersion objective (NA 1.4) and a Nikon Eclipse Ti-E inverted CSU-X1 spinning disk confocal microscope equipped with a 100x oil immersion objective (NA 1.4). The images shown are the sums of the planes containing the structure of interest. To analyze the distribution of ESCRT proteins in MBRs, Z-stack images of subconfluent cultures were acquired with a Zeiss LSM800 confocal microscope equipped with a 63x oil immersion lens (NA 1.4).

Time-lapse confocal imaging. Cells were seeded on 35-mm glass-bottom dishes as mentioned above and maintained in MEM without phenol red during recording. Time-

bioRxiv preprint doi: https://doi.org/10.1101/810523; this version posted October 20, 2019. The copyright holder for this preprint (which was not certified by peer review) is the author/funder, who has granted bioRxiv a license to display the preprint in perpetuity. It is made available under aCC-BY 4.0 International license.

lapse experiments showing midbody remnant motion were acquired with a Nikon A1R+ confocal microscope with a 60x water objective (NA 1.2). A stack containing the whole structure was captured every second using a resonant scanner, and the resulting images were deconvoluted with Huygens software (SVI) to enhance the signal-to-noise ratio. 3D reconstructions were generated in NIS-Elements software (Nikon). To quantify motion confinement, a single plane was acquired every second for 3 min with a Nikon Eclipse Ti-E inverted CSU-X1 spinning disk confocal microscope equipped with a 100x oil immersion objective (NA 1.4). The position of the structure was determined in every frame, and the geometrical center of every dataset calculated. From that point, a circle that included 95% of the points was delineated and used to calculate the length of the MBR connection.

Correlative light and scanning electron microscopy. Prior to cell seeding, 250-nm gold nanobeads (BBI Solutions) were deposited over a 35-mm glass-bottom plate pre-coated with polylysine ($1.0x10^4$ beads/mm^2) to serve as fiducial markers. Reference marks were made on the coverslip to localize the imaging area and maintain sample orientation between the two imaging methods used. Then, MDCK cells stably expressing either GFP-tubulin alone or Cherry-tubulin plus either GFP-L-CHMP4B or GFP-L-CHMP4C were seeded as described above. After 48 h of cell growth, cells were pre-fixed with a volume of 2x fixing solution (4% paraformaldehyde plus 4% glutaraldehyde in phosphate buffer) equal to that of the culture medium for 10 min at room temperature, followed by 3 h incubation with 1x fixing solution. For the confocal microscopy component, a Nikon A1R+ confocal microscope with a 60x water objective (NA 1.2) was used. First, a low-magnification image was acquired for alignment and navigation purposes, including the fluorescence signal and a reflection channel showing the position of the gold nanobeads. Candidate MBR structures selected by the absence of tubulin label at the FB sides were identified and high-resolution images were acquired when needed. The samples for SEM analysis were prepared by a gentle procedure adapted from Katsen-Globa et al. (2016) that avoids conventional treatments, such as osmium post-fixation, critical-point desiccation, and sputter coating with gold, that could alter the cell-surface topography and that are used in sample preparation for analysis under conventional SEM equipments. Briefly, the cells in the coverslisp were dehydrated by immersion in increasing concentrations of ethanol (10% increments up to 100%, 3 min per solution). After dehydration, ethanol was substituted by

bioRxiv preprint doi: https://doi.org/10.1101/810523; this version posted October 20, 2019. The copyright holder for this preprint (which was not certified by peer review) is the author/funder, who has granted bioRxiv a license to display the preprint in perpetuity. It is made available under aCC-BY 4.0 International license.

hexamethyldisilazane (HMDS, Sigma-Aldrich) by sequential 3 min incubation in a 1:1 ethanol-HMDS solution and pure HMDS. The samples were air-dried overnight. Then, the coverslip was attached to a sample holder with carbon adhesive tape and encircled with copper foil to reduce charge accumulation. Scanning electron microscopy images were acquired with ultra-high resolution FEI Verios 460 field-emission SEM equipment with a calibrated resolution below 0.6 nm at 1 keV landing energy. This equipment allows obtaining more surface detail, creating less beam damage, and reducing charging effects compared with conventional SEM equipments. Sample orientation was first adjusted using the in-chamber camera and reference marks, and the imaging area localized. A low-magnification image matching the one acquired under the confocal microscope was acquired, and the position of the gold nanobeads identified. The pattern formed by the cells over the substrate was first used for rough alignment, and the position of the gold nanobeads was then used to refine the alignment, facilitating the identification of the structures of interest. VLV SEM images of the selected structures were acquired at 1 keV with a current of 13 pA by an in-lens secondary electron detector. To observe the structure of interest from different angles, the sample stage was tilted through 45º and rotated in 30º increments (Fig. S1F). Finally, 3D reconstructions of the corresponding confocal images were generated in NIS-Elements (Nikon) and rotated to match the orientation of their corresponding SEM counterparts.

Midbody remnant characterization and size analysis. A top-view SEM image was acquired for every candidate structure identified as an MBR by CLEM. MBRs showing continuity between the plasma membrane and the end of one of the cones flanking the MB were classified as connected MBRs. For symmetry analysis, the overall size of both regions flanking the FB was considered. The actual length of the MBR long axis was calculated from distance and angle measurements taken from top-view images (Fig. S2B) as follows:

$$\alpha = \sin^{-1}\frac{2 \times (E - F)}{C - D} \qquad \beta = 90 - \alpha \qquad L = \frac{A - B}{\cos\beta}$$

Abscission timing quantification. Cells were seeded on glass-bottom 24-well plates (MatTek) and transfected with siRNA as previously described. Imaging was carried out with a 40x dry objective lens (NA 0.75) on a Nikon Ti-Eclipse wide-field inverted microscope controlled by NIS-Elements software (Nikon). Cells were kept at 37ºC and

bioRxiv preprint doi: https://doi.org/10.1101/810523; this version posted October 20, 2019. The copyright holder for this preprint (which was not certified by peer review) is the author/funder, who has granted bioRxiv a license to display the preprint in perpetuity. It is made available under aCC-BY 4.0 International license.

5% CO_2 in an environmental chamber and imaged every 10 min for 24 h. The time period between the formation of the midbody and abscission was considered as the abscission time.

Immunoprecipitation and immunoblotting. MDCK II cells stably expressing GFP-L-CHMP4C variants were lysed at 4ºC in 1 ml lysis buffer containing 50 mM Tris, pH 7.4, 150 mM NaCl, 5 mM EDTA, 5% glycerol, 1% Triton X-100 and a protease inhibitor cocktail (Merck, product 11697498001) Lysates were sonicated and centrifuged for 10 min, the cleared supernatant was then incubated with anti-GFP coupled magnetic microparticles (GFP-Trap, ChromoTek) for 2 h followed by four washing steps. Bound proteins were eluted in Laemmli's buffer and boiled before SDS-PAGE and immunoblotting.

Ciliogenesis assay. MDCK II cells were transfected with the plasmid (pSuperGFP-shCHMP4C) or an empty vector (pSuperGFPN1) using Amaxa nucleofector. $9.0x10^5$ cells were plated on 12 mm Transwell permeable supports (Corning) and cultured for 72 h. Samples were processed for immunofluorescence analysis and imaged with a Zeiss LSM510 confocal microscope equipped with a 63x oil immersion lens (NA 1.4). The percentages of ciliated cells were determined for GFP-positive and -negative cells, and used to calculate the ratio between them.

Statistical analysis. All graphs were produced and statistical analysis performed with Prism software (GraphPad). Statistical significance was assessed with a two-tailed Student's unpaired t-test. Additional information is shown in figure legends.

ACKNOWLEDGEMENTS

The expert technical advice of the Optical and Confocal Microscopy Facility of CBMSO is gratefully acknowledged. We thank Dr Phil Mason for revising the English language of the manuscript, Laura Fernandez-Martín for invaluable technical help and David Esteban-Mendoza for his contribution to optimization of the SEM protocol. This work was supported by a grant (PGC2018-095643-B-I00) to MAA from the Spanish Ministerio de Ciencia, Innovación y Universidades, Agencia Estatal de Investigación, y Fondo Europeo de Desarrollo Regional, European Union (MCIU/AEI/FEDER, UE), and by Wellcome Trust funding (WT102871MA) to JM-S. We also acknowledge the Micro and Nanofabrication Laboratory of the Instituto de Micro y Nanotecnología (MiNa), which is funded by the Comunidad de Madrid

bioRxiv preprint doi: https://doi.org/10.1101/810523; this version posted October 20, 2019. The copyright holder for this preprint (which was not certified by peer review) is the author/funder, who has granted bioRxiv a license to display the preprint in perpetuity. It is made available under aCC-BY 4.0 International license.

(S2018/NMT-4291 TEC2SPACE), MCIU (project CSIC13-4E-1794) and EU (FEDER, FSE), for invaluable help on SEM. A contract from MCIU (FPU14/00295) and a short-term fellowship from EMBO to JC-A are also acknowledged. The authors declare no competing interests.

bioRxiv preprint doi: https://doi.org/10.1101/810523; this version posted October 20, 2019. The copyright holder for this preprint (which was not certified by peer review) is the author/funder, who has granted bioRxiv a license to display the preprint in perpetuity. It is made available under aCC-BY 4.0 International license.

References

Agromayor, M. & Martin-Serrano, J. 2013. Knowing when to cut and run: mechanisms that control cytokinetic abscission. *Trends Cell Biol,* 23**,** 433-41. doi: 10.1016/j.tcb.2013.04.006.

Bajorek, M., Morita, E., Skalicky, J. J., Morham, S. G., Babst, M. & Sundquist, W. I. 2009. Biochemical analyses of human IST1 and its function in cytokinesis. *Mol Biol Cell,* 20**,** 1360-73. doi: 10.1091/mbc.E08-05-0475.

Bernabe-Rubio, M., Andres, G., Casares-Arias, J., Fernandez-Barrera, J., Rangel, L., Reglero-Real, N., Gershlick, D. C., Fernandez, J. J., Millan, J., Correas, I., Miguez, D. G. & Alonso, M. A. 2016. Novel role for the midbody in primary ciliogenesis by polarized epithelial cells. *J Cell Biol,* 214**,** 259-73. doi: 10.1083/jcb.201601020.

Bernabé-Rubio, M., Bosch-Fortea, M., García, E., de la Serna, J. B. & Alonso, M. A. 2019. The ciliary membrane of polarized epithelial cells stems from a midbody remnant-associated membrane patch with condensed nanodomains. *bioRxiv***,** 667642. doi: 10.1101/667642.

Byers, B. & Abramson, D. H. 1968. Cytokinesis in HeLa: post-telophase delay and microtubule-associated motility. *Protoplasma,* 66**,** 413-35.

Caballe, A., Wenzel, D. M., Agromayor, M., Alam, S. L., Skalicky, J. J., Kloc, M., Carlton, J. G., Labrador, L., Sundquist, W. I. & Martin-Serrano, J. 2015. ULK3 regulates cytokinetic abscission by phosphorylating ESCRT-III proteins. *Elife,* 4**,** e06547. doi: 10.7554/eLife.06547.

Capalbo, L., Montembault, E., Takeda, T., Bassi, Z. I., Glover, D. M. & D'Avino, P. P. 2012. The chromosomal passenger complex controls the function of endosomal sorting complex required for transport-III Snf7 proteins during cytokinesis. *Open Biol,* 2**,** 120070. doi: 10.1098/rsob.120070.

Carlton, J. G., Caballe, A., Agromayor, M., Kloc, M. & Martin-Serrano, J. 2012. ESCRT-III governs the Aurora B-mediated abscission checkpoint through CHMP4C. *Science,* 336**,** 220-5. doi: 10.1126/science.1217180.

Carlton, J. G. & Martin-Serrano, J. 2007. Parallels between cytokinesis and retroviral budding: a role for the ESCRT machinery. *Science,* 316**,** 1908-12. doi: 10.1126/science.1143422.

Chen, C. T., Ettinger, A. W., Huttner, W. B. & Doxsey, S. J. 2013. Resurrecting remnants: the lives of post-mitotic midbodies. *Trends Cell Biol,* 23**,** 118-28. doi: 10.1016/j.tcb.2012.10.012.

Crowell, E. F., Gaffuri, A. L., Gayraud-Morel, B., Tajbakhsh, S. & Echard, A. 2014. Engulfment of the midbody remnant after cytokinesis in mammalian cells. *J Cell Sci,* 127**,** 3840-51. doi: 10.1242/jcs.154732.

bioRxiv preprint doi: https://doi.org/10.1101/810523; this version posted October 20, 2019. The copyright holder for this preprint (which was not certified by peer review) is the author/funder, who has granted bioRxiv a license to display the preprint in perpetuity. It is made available under aCC-BY 4.0 International license.

Dionne, L. K., Wang, X. J. & Prekeris, R. 2015. Midbody: from cellular junk to regulator of cell polarity and cell fate. *Curr Opin Cell Biol,* 35**,** 51-8. doi: 10.1016/j.ceb.2015.04.010.

Elia, N., Fabrikant, G., Kozlov, M. M. & Lippincott-Schwartz, J. 2012. Computational model of cytokinetic abscission driven by ESCRT-III polymerization and remodeling. *Biophys J,* 102**,** 2309-20. doi: 10.1016/j.bpj.2012.04.007.

Elia, N., Sougrat, R., Spurlin, T. A., Hurley, J. H. & Lippincott-Schwartz, J. 2011. Dynamics of endosomal sorting complex required for transport (ESCRT) machinery during cytokinesis and its role in abscission. *Proc Natl Acad Sci U S A,* 108**,** 4846-51. doi: 10.1073/pnas.1102714108.

Ettinger, A. W., Wilsch-Brauninger, M., Marzesco, A. M., Bickle, M., Lohmann, A., Maliga, Z., Karbanova, J., Corbeil, D., Hyman, A. A. & Huttner, W. B. 2011. Proliferating versus differentiating stem and cancer cells exhibit distinct midbody-release behaviour. *Nat Commun,* 2**,** 503. doi: 10.1038/ncomms1511.

Fededa, J. P. & Gerlich, D. W. 2012. Molecular control of animal cell cytokinesis. *Nat Cell Biol,* 14**,** 440-7. doi: 10.1038/ncb2482.

Fremont, S. & Echard, A. 2017. Studying cytokinesis and midbody remnants using correlative light/scanning EM. *Methods Cell Biol,* 137**,** 239-251. doi: 10.1016/bs.mcb.2016.03.028.

Gerdes, J. M., Davis, E. E. & Katsanis, N. 2009. The vertebrate primary cilium in development, homeostasis, and disease. *Cell,* 137**,** 32-45. doi: 10.1016/j.cell.2009.03.023.

Goliand, I., Adar-Levor, S., Segal, I., Nachmias, D., Dadosh, T., Kozlov, M. M. & Elia, N. 2018. Resolving ESCRT-III spirals at the intercellular bridge of dividing cells using 3D STORM. *Cell Rep,* 24**,** 1756-1764. doi: 10.1016/j.celrep.2018.07.051.

Ishikawa, H. & Marshall, W. F. 2011. Ciliogenesis: building the cell's antenna. *Nat Rev Mol Cell Biol,* 12**,** 222-34. doi: 10.1038/nrm3085.

Katsen-Globa, A., Puetz, N., Gepp, M. M., Neubauer, J. C. & Zimmermann, H. 2016. Study of SEM preparation artefacts with correlative microscopy: Cell shrinkage of adherent cells by HMDS-drying. *Scanning,* 38**,** 625-633. doi: 10.1002/sca.21310.

Kuo, T. C., Chen, C. T., Baron, D., Onder, T. T., Loewer, S., Almeida, S., Weismann, C. M., Xu, P., Houghton, J. M., Gao, F. B., Daley, G. Q. & Doxsey, S. 2011. Midbody accumulation through evasion of autophagy contributes to cellular reprogramming and tumorigenicity. *Nat Cell Biol,* 13**,** 1214-23. doi: 10.1038/ncb2332.

Lujan, P., Rubio, T., Varsano, G. & Kohn, M. 2017. Keep it on the edge: The post-mitotic midbody as a polarity signal unit. *Commun Integr Biol,* 10**,** e1338990. doi: 10.1080/19420889.2017.1338990.

bioRxiv preprint doi: https://doi.org/10.1101/810523; this version posted October 20, 2019. The copyright holder for this preprint (which was not certified by peer review) is the author/funder, who has granted bioRxiv a license to display the preprint in perpetuity. It is made available under aCC-BY 4.0 International license.

Mierzwa, B. & Gerlich, D. W. 2014. Cytokinetic abscission: molecular mechanisms and temporal control. *Dev Cell,* 31**,** 525-38. doi: 10.1016/j.devcel.2014.11.006.

Morita, E., Sandrin, V., Chung, H. Y., Morham, S. G., Gygi, S. P., Rodesch, C. K. & Sundquist, W. I. 2007. Human ESCRT and ALIX proteins interact with proteins of the midbody and function in cytokinesis. *EMBO J,* 26**,** 4215-27. doi: 10.1038/sj.emboj.7601850.

Ou, G., Gentili, C. & Gonczy, P. 2014. Stereotyped distribution of midbody remnants in early C. elegans embryos requires cell death genes and is dispensable for development. *Cell Res,* 24**,** 251-3. doi: 10.1038/cr.2013.140.

Rodriguez-Boulan, E., Kreitzer, G. & Musch, A. 2005. Organization of vesicular trafficking in epithelia. *Nat Rev Mol Cell Biol,* 6**,** 233-47. doi: 10.1038/nrm1593.

Sadler, J. B. A., Wenzel, D. M., Williams, L. K., Guindo-Martinez, M., Alam, S. L., Mercader, J. M., Torrents, D., Ullman, K. S., Sundquist, W. I. & Martin-Serrano, J. 2018. A cancer-associated polymorphism in ESCRT-III disrupts the abscission checkpoint and promotes genome instability. *Proc Natl Acad Sci U S A,* 115**,** E8900-E8908. doi: 10.1073/pnas.1805504115.

Schiel, J. A., Park, K., Morphew, M. K., Reid, E., Hoenger, A. & Prekeris, R. 2011. Endocytic membrane fusion and buckling-induced microtubule severing mediate cell abscission. *J Cell Sci,* 124**,** 1411-24. doi: 10.1242/jcs.081448.

Schoneberg, J., Lee, I. H., Iwasa, J. H. & Hurley, J. H. 2017. Reverse-topology membrane scission by the ESCRT proteins. *Nat Rev Mol Cell Biol,* 18**,** 5-17. doi: 10.1038/nrm.2016.121.

Sherman, S., Kirchenbuechler, D., Nachmias, D., Tamir, A., Werner, S., Elbaum, M. & Elia, N. 2016. Resolving new ultrastructural features of cytokinetic abscission with soft-X-ray cryo-tomography. *Sci Rep,* 6**,** 27629. doi: 10.1038/srep27629.

Singla, V. & Reiter, J. F. 2006. The primary cilium as the cell's antenna: signaling at a sensory organelle. *Science,* 313**,** 629-33. doi: 10.1126/science.1124534.

Ventimiglia, L. N., Cuesta-Geijo, M. A., Martinelli, N., Caballe, A., Macheboeuf, P., Miguet, N., Parnham, I. M., Olmos, Y., Carlton, J. G., Weissenhorn, W. & Martin-Serrano, J. 2018. CC2D1B coordinates ESCRT-III activity during the mitotic reformation of the nuclear envelope. *Dev Cell,* 47**,** 547-563 e6. doi: 10.1016/j.devcel.2018.11.012.

Wuhrer, R. & Moran, K. 2016. Low voltage imaging and X-ray microanalysis in the SEM: challenges and opportunities. *IOP Conference Series: Materials Science and Engineering,* 109**,** 012019. doi: 10.1088/1757-899x/109/1/012019.

bioRxiv preprint doi: https://doi.org/10.1101/810523; this version posted October 20, 2019. The copyright holder for this preprint (which was not certified by peer review) is the author/funder, who has granted bioRxiv a license to display the preprint in perpetuity. It is made available under aCC-BY 4.0 International license.

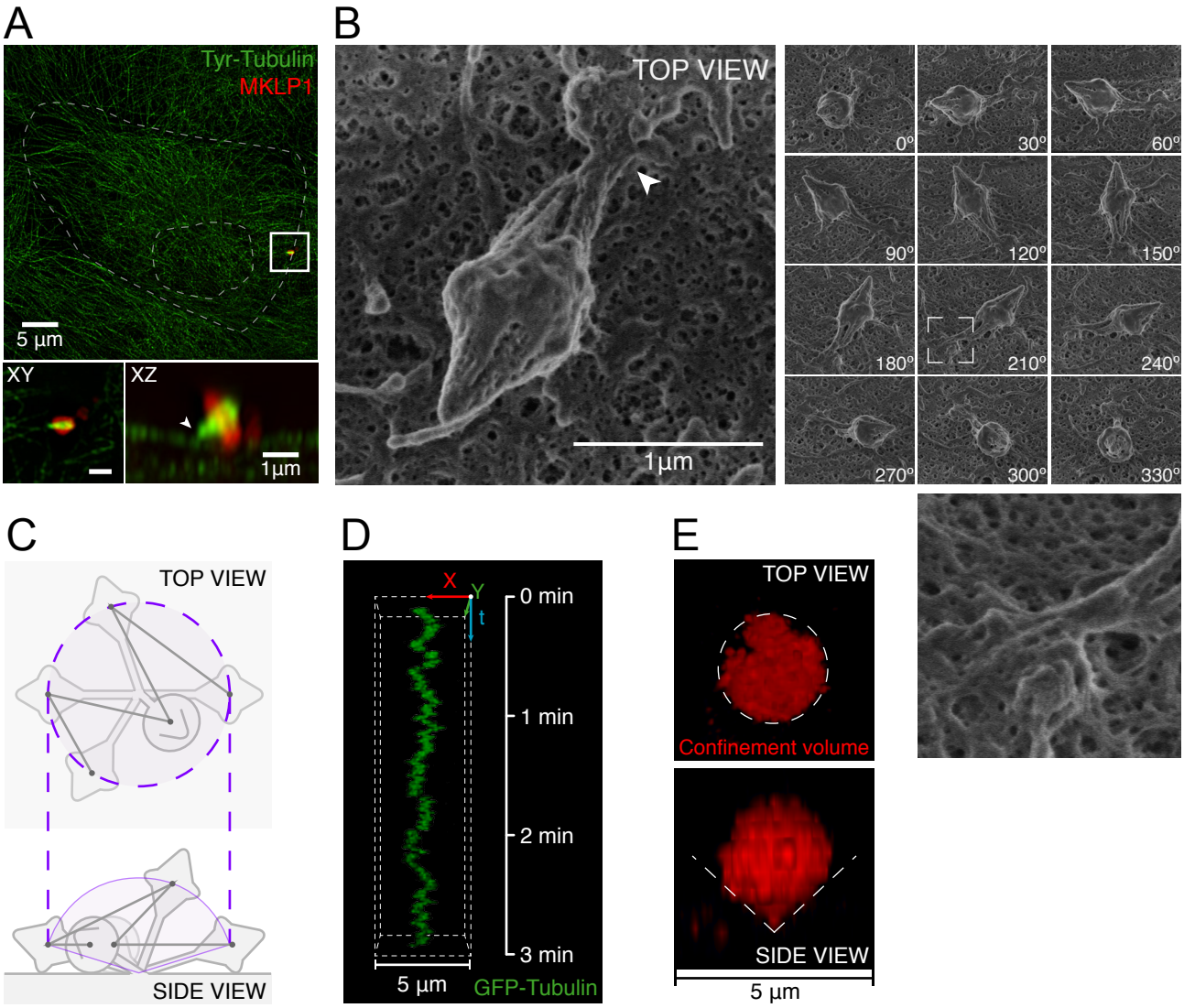

Figure 1. **The MBR is on the surface of MDCK cells**. (**A**) An MBR as seen by super-resolution confocal microscopy in cells stained for tyrosinated α-tubulin and the FB marker MKLP1 (top panel). Dashed lines indicate cell and nuclear contours. The enlargement of the boxed region shows the characteristic ring-like structure of the FB flanked by microtubules, as seen in both XY and XZ views (bottom panels). The arrowhead indicates the absence of microtubule bundles in the cytoplasmic region adjacent to the MBR. (**B**) Images of a connected MBR on the plasma membrane as observed by SEM in top (left panels) and side views (middle right panels). Numbers indicate the angle of rotation of the sample stage. The arrowhead shows the connection point. The boxed region was enlarged to show the existence of continuity between the MBR membrane and the plasma membrane (bottom panel). The conical structures at the sides of the FB are of similar length and, therefore, this MBR is shown as representative of symmetrical connected MBRs. (**C-E**) Graphical representation in top and side views of the confinement volume in which MBR movement is restricted (C). (D) Kymograph showing a 3D reconstruction of the movement of an MBR, as visualized with GFP-tubulin, over time in a live cell. (E) Top and side views of the funnel-shaped confinement volume calculated from the same MBR. See also Fig. S1 and Video 1.

bioRxiv preprint doi: https://doi.org/10.1101/810523; this version posted October 20, 2019. The copyright holder for this preprint (which was not certified by peer review) is the author/funder, who has granted bioRxiv a license to display the preprint in perpetuity. It is made available under aCC-BY 4.0 International license.

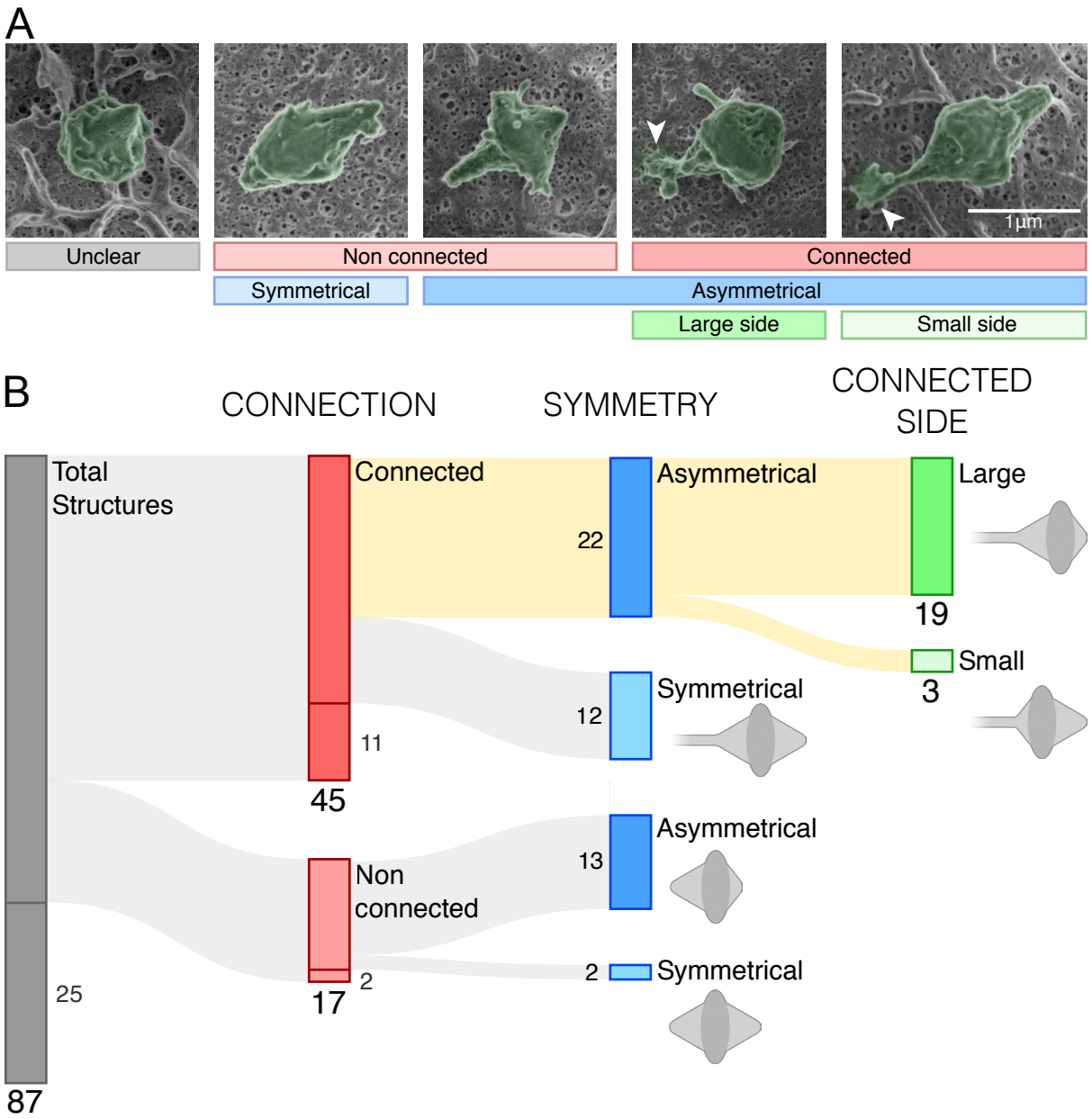

Figure 2. **Most MBRs remain physically connected to the plasma membrane**. (**A**) Representative examples of MBR morphologies others than those shown in Fig. 1. Arrowheads indicate connection points. (**B**) Sankey diagram showing the results of our MBR morphology analysis. Large and small sized numbers indicate the population size of each class and of the subclasses, respectively. See also Fig. S2.

bioRxiv preprint doi: https://doi.org/10.1101/810523; this version posted October 20, 2019. The copyright holder for this preprint (which was not certified by peer review) is the author/funder, who has granted bioRxiv a license to display the preprint in perpetuity. It is made available under aCC-BY 4.0 International license.

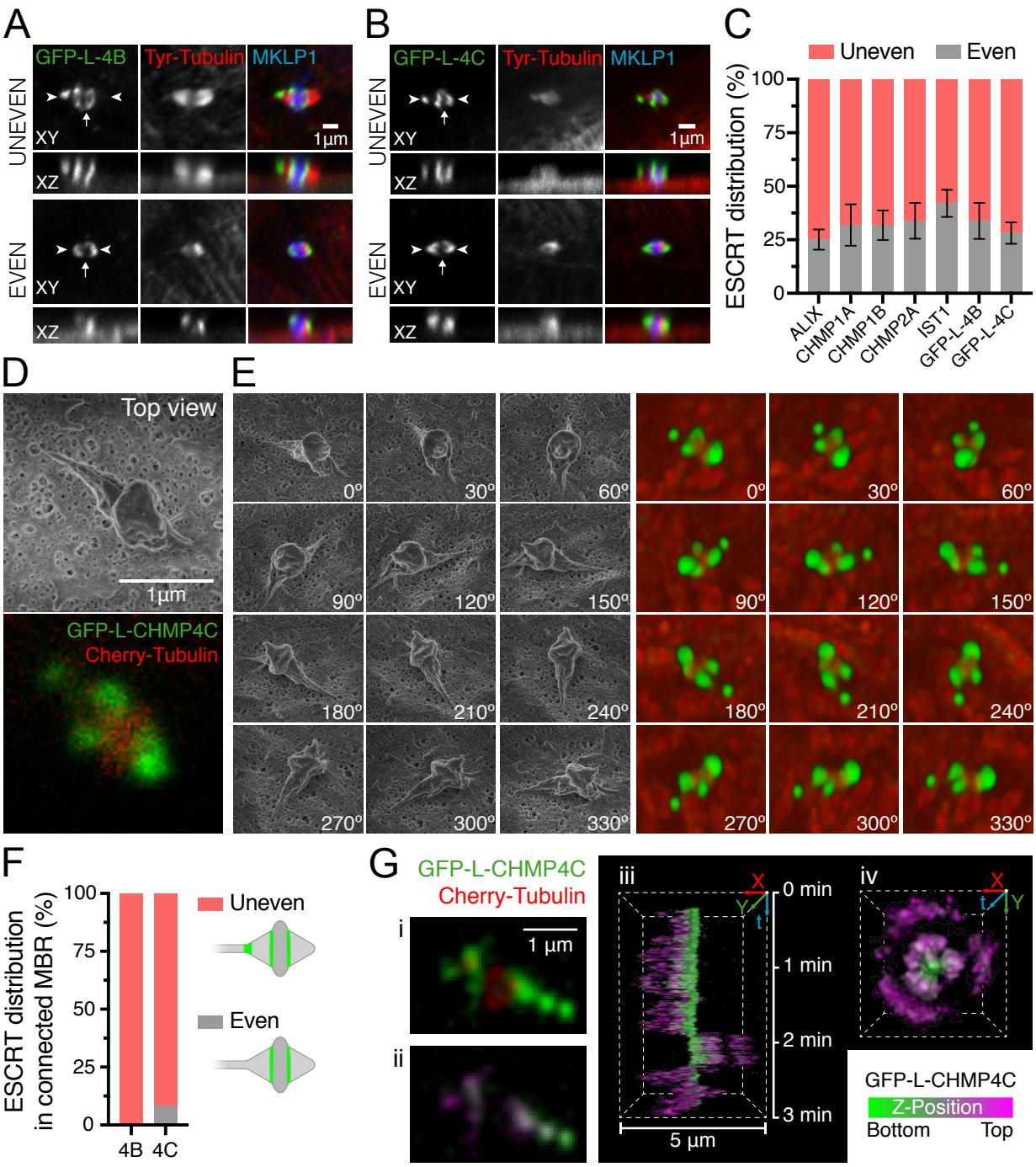

Figure 3. **The ESCRT machinery locates to the membranous connection between the MBR and the plasma membrane**. (**A-C**) Distribution of GFP-L-CHMP4B (GFP-L-4B) (A) and GFP-L-CHMP4C (GFP-L-4C) (B) at the MBR. XY and XZ views of MBRs with uneven (top panels) and even (bottom panels) distribution of these markers. The arrow and the arrowheads in A and B indicate the FB and the MBR tips, respectively. (C) Histogram showing the percentage of MBRs with uneven and even distribution for GFP-L-CHMP4B, GFP-L-CHMP4C and a panel of endogenous ESCRT markers. Data are summarized as the mean ± SD from three independent experiments (n=29-93). (**D, E**) CLEM images showing the presence of GFP-L-CHMP4C at the connection of the MBR with the plasma membrane. (D) Top-view image of a connected MBR acquired by SEM (top) and confocal microscopy (bottom). (E) Side view SEM images (left panels) and matching confocal images obtained by 3D reconstruction (right). Numbers indicate the angle of sample-stage rotation. (**F**) Quantification of GFP-L-CHMP4B and GFP-L-CHMP4C distribution in connected MBRs as observed by CLEM (n=16 and 18, respectively). (**G**) Tracks of GFP-L-CHMP4C and Cherry-tubulin movement of an MBR in a live cell. (i) GFP-L-CHMP4C and Cherry-tubulin distribution in an MBR; (ii) image of the distribution GFP-L-CHMP4C using the indicated depth-color scale; (iii and iv) 3D reconstructions of the movement followed by the MBR over a 3-min period. See also Fig. S3 and Video 2.

bioRxiv preprint doi: https://doi.org/10.1101/810523; this version posted October 20, 2019. The copyright holder for this preprint (which was not certified by peer review) is the author/funder, who has granted bioRxiv a license to display the preprint in perpetuity. It is made available under aCC-BY 4.0 International license.

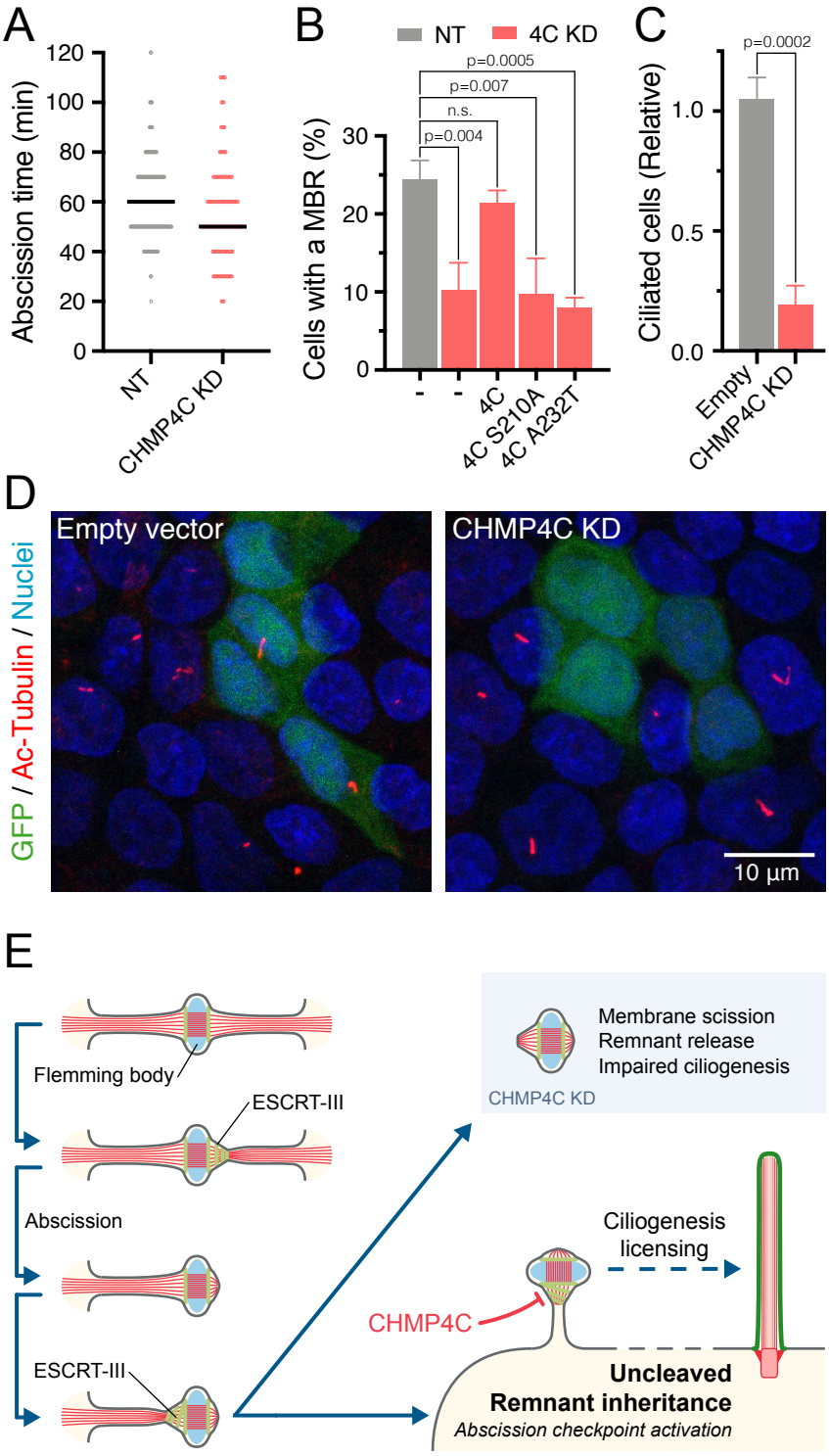

Figure 4. **CHMP4C is required for MBR inheritance and primary ciliogenesis**. (**A**) The time between the formation of the midbody and abscission was measured in control (gray points) and siRNA-mediated CHMP4C-knockdown (KD) cells (red points). Three independent experiments (n=27-159 in control cells; n=8-95 in CHMP4C KD cells) were performed. Black bars represent median values. (**B**) Percentage of cells with an MBR in control (gray bar) and siRNA-mediated CHMP4C-KD cells (red bars) expressing the indicated exogenous CHMP4 proteins (n=2714-3447 cells for control and n=800-1463 for KD cells). (**C**) Effect of CHMP4C knockdown on the frequency of ciliated cells. The number of cells with a primary cilium in cells expressing GFP alone or both GFP and shCHMP4C was expressed relative to that of non-transfected cells (n=77-88 for control; n=70-161 for CHMP4C KD cells). (**D**) Representative fields of cells expressing GFP alone, or both GFP and shCHMP4C stained for acetylated tubulin to visualize the primary cilium. The mean ± SD from three independent experiments are shown in (B, C). Probabilities are those associated with unpaired two-tailed Student's t-tests. (**E**) Schematic model. CHMP4C delays the cleavage of the intact MB arm after abscission and doing so determines the fate of the MBR. An MBR that is physically connected to the plasma membrane is the MBR form used by the cell to prepare the centrosome for primary cilium formation. See also Fig. S4.

bioRxiv preprint doi: https://doi.org/10.1101/810523; this version posted October 20, 2019. The copyright holder for this preprint (which was not certified by peer review) is the author/funder, who has granted bioRxiv a license to display the preprint in perpetuity. It is made available under aCC-BY 4.0 International license.

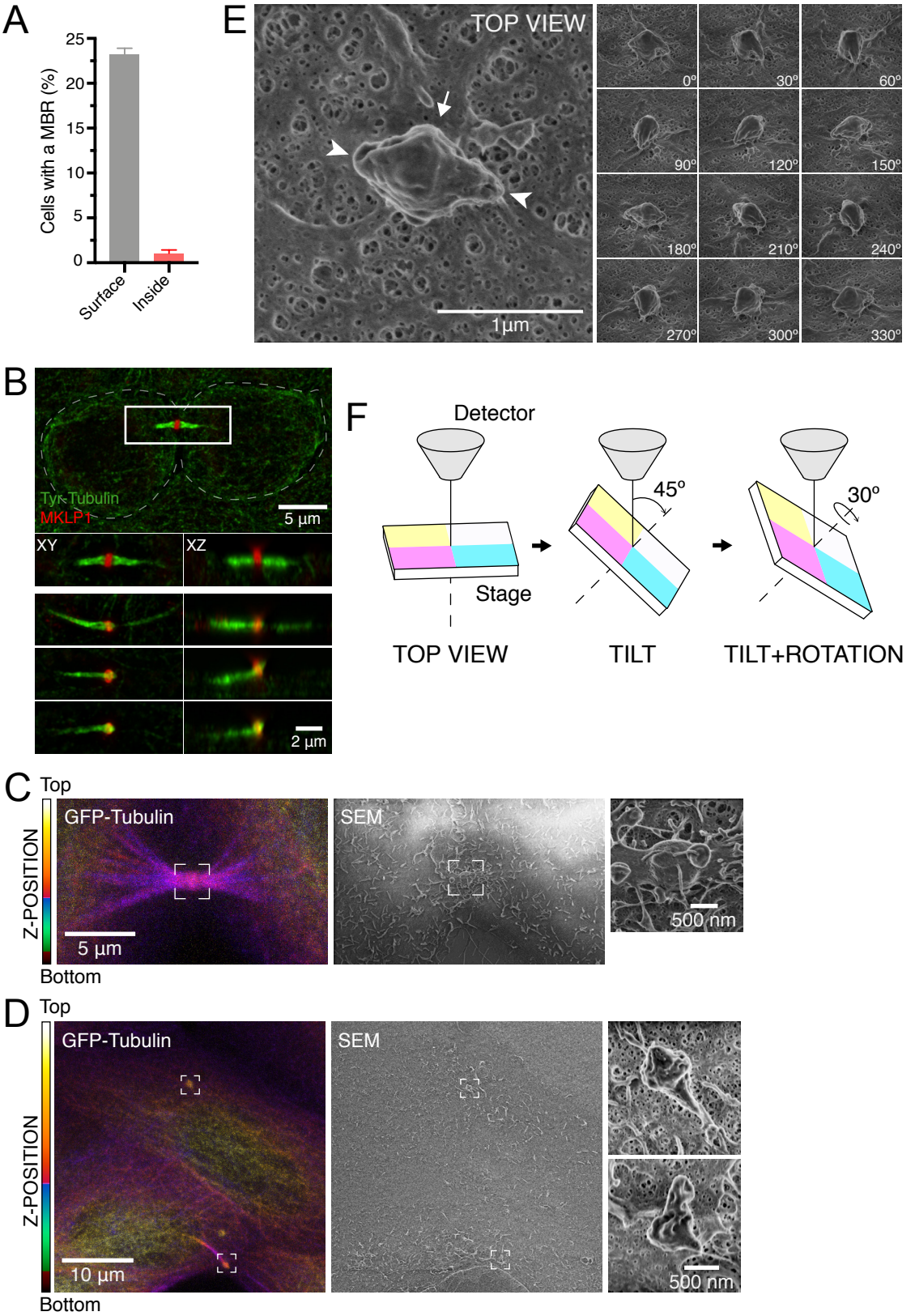

Figure S1. **Localization of MBRs in MDCK cells**. (**A**) The surface or intracellular localization of MBRs was analyzed by confocal microscopy. Data are summarized as the mean ± SD of the percentage of cells with an MBR from three independent experiments (n=285-296 cells). (**B**) Cytokinetic stages observed by super-resolution confocal microscopy. Panoramic view of two sister cells connected by an MB (top panel) and enlargement of the MB region before and immediately after abscission (bottom panels). The dashed line delineates the cell contour. Note the microtubule bundles flanking the FB. (**C, D**) Examples of CLEM imaging. Images of an MB before (C) and after abscission (D). Confocal depth-coded color images of GFP-tubulin distribution (left), the corresponding SEM images (center), and enlargement of the boxed region that contains the structure of interest. The color scale used is indicated. (**E**) Image of a non-connected MBR on the plasma membrane as observed by SEM in top (left panels) and side views (right). Numbers indicate the angle of rotation of the sample stage. The arrow and the arrowheads indicate the FB and the MBR tips, respectively. (**F**) Procedure of side view image acquisition by SEM using tilting and rotation of the sample stage.

bioRxiv preprint doi: https://doi.org/10.1101/810523; this version posted October 20, 2019. The copyright holder for this preprint (which was not certified by peer review) is the author/funder, who has granted bioRxiv a license to display the preprint in perpetuity. It is made available under aCC-BY 4.0 International license.

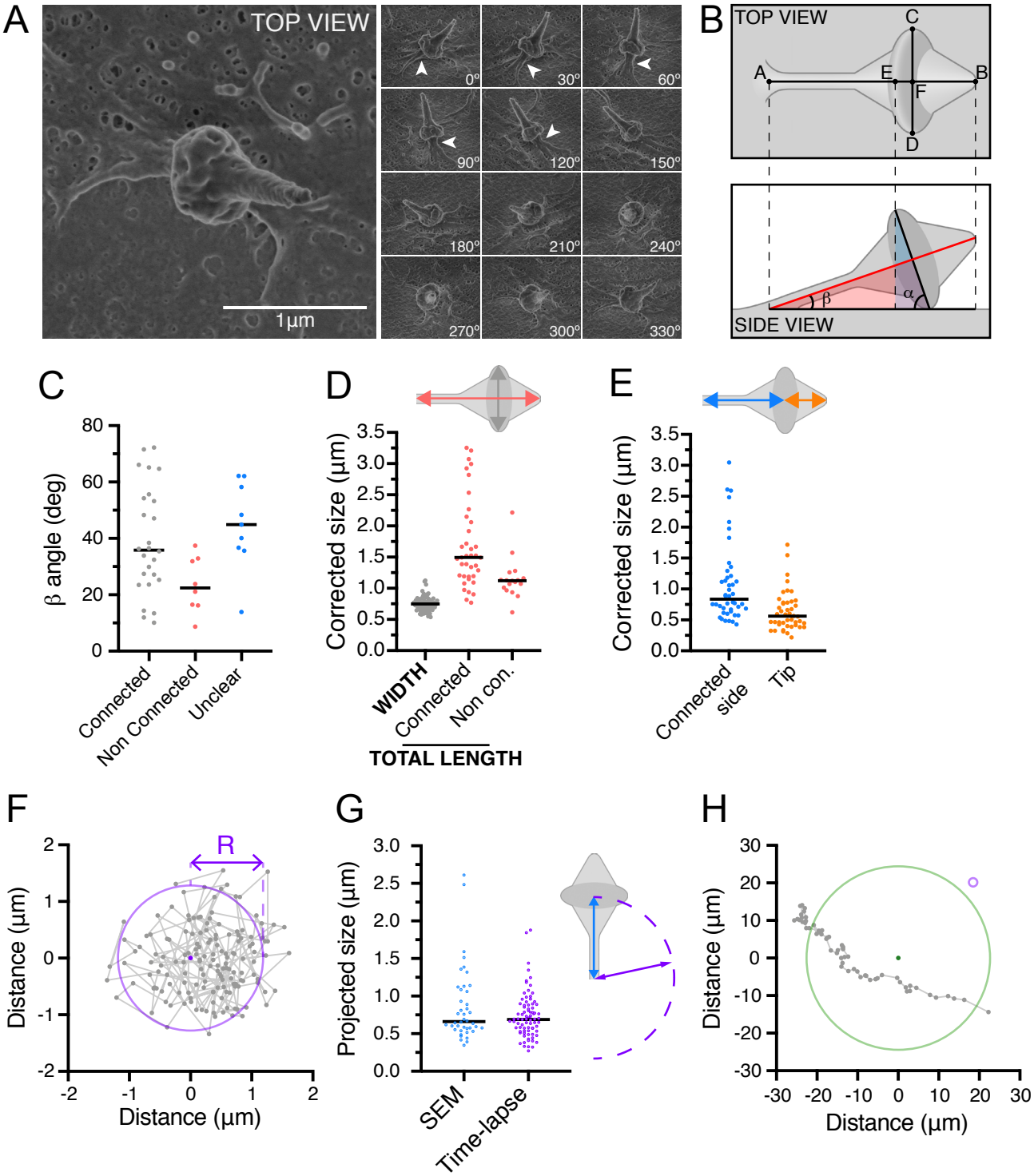

Figure S2. **Quantification of MBR size**. (**A**) Top-view image of an example of an MBR classified as an unclear case (left). The tilt series reveals that the MBR is connected to the plasma membrane (arrowheads; right panels). (**B**) Schematic illustrating how MBRs appear in top- and side-view images. MBR width was defined as the major axis of the FB (C-D line). The projected length of the long axis of the MBR is the distance between the two ends of the structure (A-B line). The intersection of the two lines defines the center of the FB (point F), which allows the measurement of the projected distance (A-F line) between the connection point and the center of the FB. The inclination angle (β) of the MBR with respect to the cell surface was derived from the inclination angle of the FB large axis (α), which was calculated from the distance between the FB rim (point E) and its center (point F). (**C**) β angle values for MBRs classified as connected, non-connected and unclear. Black bars represent median values. (**D**) Quantification of FB width (n=87) and total MBR length of connected (n=38) and non-connected (n=17) structures. (**E**) Length of the two sides flanking the FB in connected MBRs (n=38). Black bars indicate median values. (**F**) Example of the trajectory followed by an MBR. The purple dot represents the center of the trajectory. The circumference includes 95% of the dots. (**G**) Measurements of the projected distance between the connection point and the FB by SEM (n=42) compared with that calculated by the analysis of MBR trajectories obtained from time-lapse experiments (n=81). (**H**) Trajectory followed by a released MBR. The purple circle was drawn to be the same size as that in (F). Black bars represent median values.

bioRxiv preprint doi: https://doi.org/10.1101/810523; this version posted October 20, 2019. The copyright holder for this preprint (which was not certified by peer review) is the author/funder, who has granted bioRxiv a license to display the preprint in perpetuity. It is made available under aCC-BY 4.0 International license.

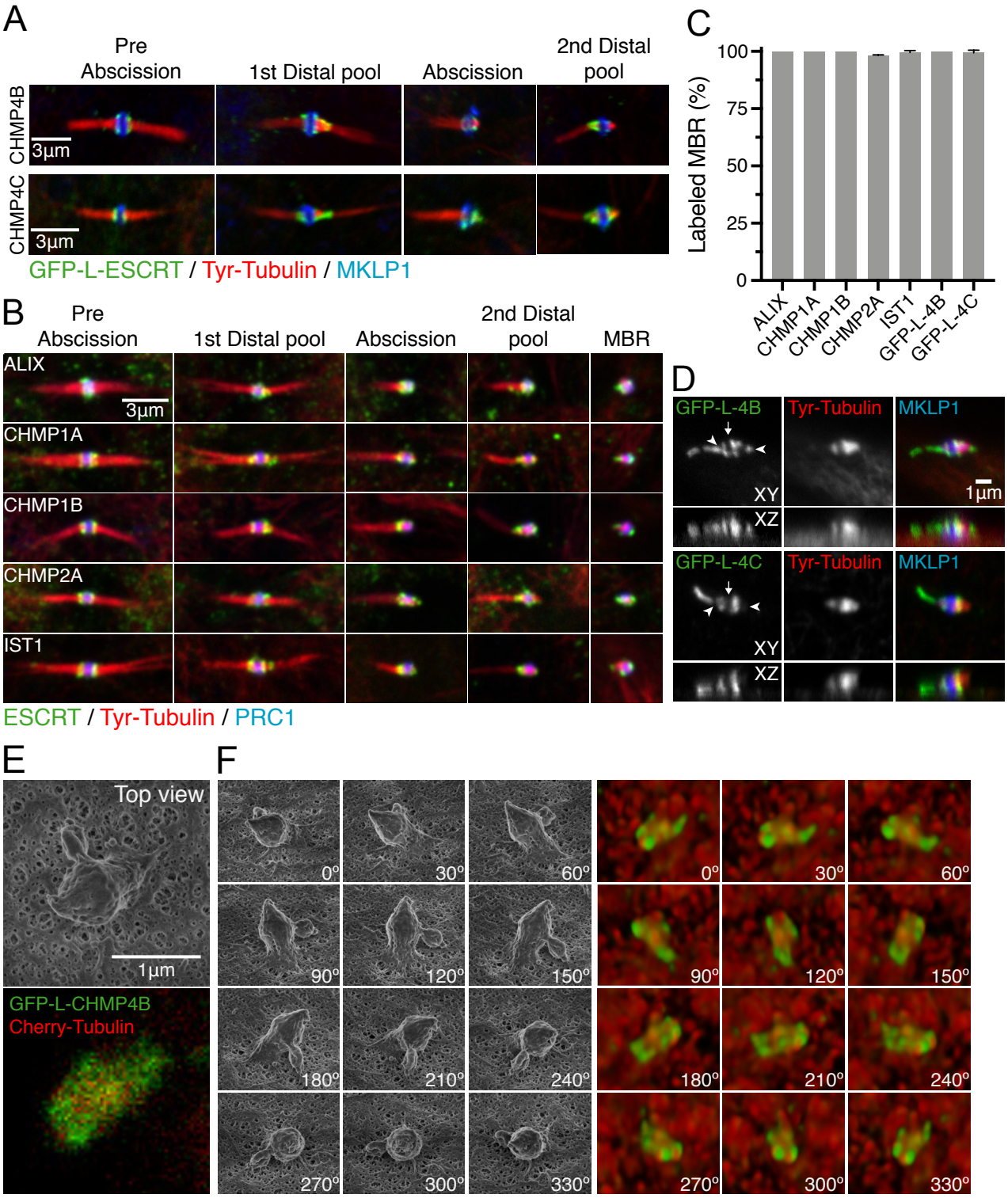

Figure S3. **Distribution of ESCRT proteins at the MB and at the connection of the MBR with the plasma membrane**. (**A-C**) Localization of GFP-L-CHMP4B and GFP-L-CHMP4C (A) and a panel of endogenous ESCRT proteins (B) at different stages of cytokinesis. (C) Percentage of MBRs positive for the indicated ESCRT proteins. The histogram represents the mean ± SD from three independent experiments (n=35-139). (**D**) Examples of MBRs showing uneven ESCRT distribution with an elongated pool of GFP-L-CHMP4B (top) and GFP-L-CHMP4C (bottom) in XY and XZ views. The arrow and the arrowheads indicate the FB and the MBR tips, respectively. (**E, F**) CLEM images showing the localization of GFP-L-CHMP4B at the connection between the MBR and the plasma membrane. (E) Top-view images of the same connected MBR acquired by SEM (top) and confocal microscopy (bottom). (F) Tilt series of SEM images (left) and the corresponding 3D reconstruction of the confocal images (right). Numbers indicate the rotation angle of the sample stage.

bioRxiv preprint doi: https://doi.org/10.1101/810523; this version posted October 20, 2019. The copyright holder for this preprint (which was not certified by peer review) is the author/funder, who has granted bioRxiv a license to display the preprint in perpetuity. It is made available under aCC-BY 4.0 International license.

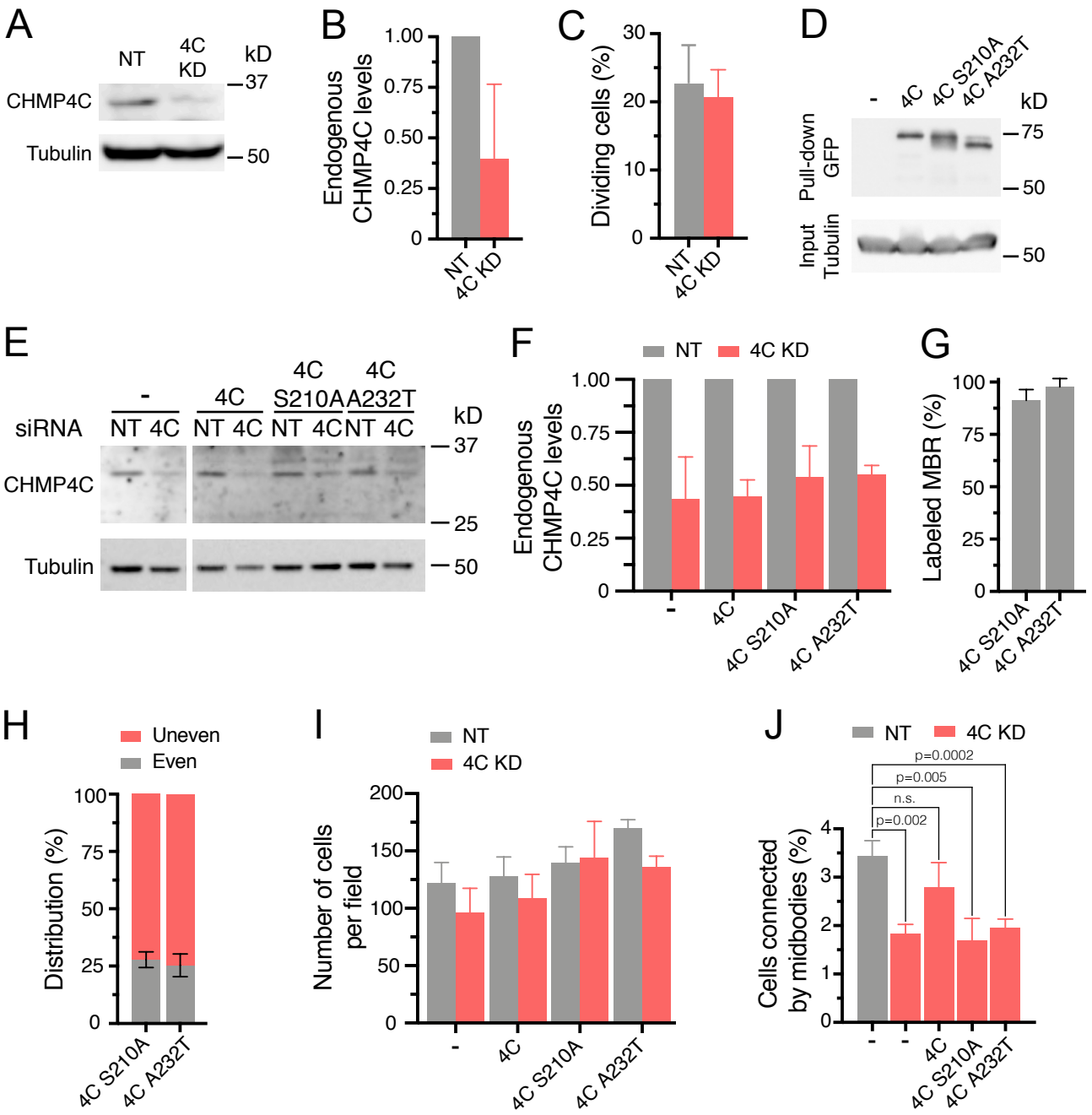

Figure S4. **Effect of CHMP4C knockdown on the percentages of dividing cells and cells connected by an MB**. (**A, B**) Representative immunoblot showing the effect of siCHMP4C on endogenous CHMP4C levels for the experiments shown in Fig. 4A and S4C (A). (B) Quantification of CHMP4C KD by siCHMP4C. The histogram represents the levels of CHMP4C in siCHMP4C-transfected cells relative to cells transfected with control siNT. (**C**) Effect of CHMP4C KD on the frequency of dividing cells as determined by time-lapse experiments. The histogram represents the percentage of dividing cells relative to the initial number of cells. Three independent experiments (n=27-159 in control cells; n=8-95 in CHMP4C KD cells) were performed. (**D**) Immunoblot of a GFP-trap experiment showing the relative expression levels of the indicated GFP-fused CHMP4C proteins. (**E, F**) Representative immunoblot (E) and quantification of endogenous CHMP4C levels (F) of siCHMP4-transfected cells expressing the indicated CHMP4C exogenous proteins for the experiments shown in Fig. 4B and S4I, J. (**G, H**) Percentage of MBRs positive for the indicated CHMP4C mutants (n=58-80) (G). (H) Even or uneven distribution of the CHMP4C mutants in the MBR (n=37-56). (**I, J**) Total number of cells per field (I) and percentage of cells connected by an MB (J) in control cells and CHMP4C KD cells expressing the indicated exogenous CHMP4C proteins. The histograms in (B, C, F-J) show the mean ± SD from three independent experiments.

bioRxiv preprint doi: https://doi.org/10.1101/810523; this version posted October 20, 2019. The copyright holder for this preprint (which was not certified by peer review) is the author/funder, who has granted bioRxiv a license to display the preprint in perpetuity. It is made available under aCC-BY 4.0 International license.

Video 1. **MBR movement on the apical surface**. 3D analysis of the movement of an MBR in a live cell expressing GFP-tubulin.

Video 2. **GFP-L-CHMP4C and Cherry-tubulin distribution in a moving MBR**. (Left) GFP-L-CHMP4C and Cherry-tubulin fluorescence. (Right) The GFP-L-CHMP4C signal was pseudocolored using the indicated depth-color scale.